# Updated MISR Dark-Water Research Aerosol Retrieval Algorithm Part 1: Coupled 1.1 km Ocean-Surface Chlorophyll-a Retrievals with Empirical Calibration Corrections

5   James A. Limbacher[1,2] and Ralph A. Kahn[1]

[1]Earth Science Division, NASA Goddard Space Flight Center, Greenbelt, 20771, USA
[2]Science Systems and Applications Inc., Lanham, 20706, USA

*Correspondence to*: Ralph A. Kahn (ralph.a.kahn@nasa.gov)

**Abstract.**   As aerosol amount and type are key factors in the "atmospheric correction" required for remote-sensing
10   chlorophyll-a concentration (*Chl*) retrievals, the Multi-Angle Imaging SpectroRadiometer (MISR) can contribute to ocean color analysis despite a lack of spectral channels optimized for this application. Conversely, an improved ocean-surface constraint should also improve MISR aerosol-type products, especially spectral single-scattering albedo retrievals. We introduce a coupled, self-consistent retrieval of *Chl* together with aerosol over dark water.  There are time-varying MISR radiometric calibration errors that significantly affect key spectral reflectance ratios used in the retrievals.  Therefore, we also
15   develop and apply new calibration corrections to the MISR top-of-atmosphere (TOA) reflectance data, based on comparisons with coincident MODIS observations and trend analysis of the MISR TOA bidirectional reflectance factors (BRFs) over three pseudo-invariant desert sites.

We run the MISR Research Retrieval Algorithm (RA) with the corrected MISR reflectances to generate MISR-retrieved *Chl* and compare the MISR *Chl* values to a set of 49 coincident SeaBASS *in situ* observations. Where $Chl_{in\ situ} < 1.5$ mg m$^{-3}$, the
20   results from our *Chl* model are expected to be of highest quality, due to algorithmic assumption validity.  Comparing MISR RA *Chl* to the 49 coincident SeaBASS observations, we report a correlation coefficient (r) of 0.86, a root-mean-squared-error (RMSE) of 0.25, and a median absolute error (MAE) of 0.10.  Statistically, a two-sample Kolmogorov-Smirnov test indicates that it is not possible to distinguish between MISR *Chl*, and available SeaBASS *in situ Chl* values (p>0.1). We also compare MODIS-Terra and MISR RA *Chl* statistically, over much broader regions.  With about 1.5 million MISR-MODIS
25   collocations having MODIS *Chl* < 1.5 mg m$^{-3}$, MISR and MODIS show very good agreement: r=0.96, MAE=0.09, and RMSE=0.15.

The new dark water aerosol/*Chl* RA can retrieve *Chl* in low-*Chl*, case I waters, independent of other imagers such as MODIS, via a largely physical algorithm, compared to the commonly applied statistical ones.  At a minimum, MISR's multi-angle data should help reduce uncertainties in the MODIS Terra Ocean color retrieval where coincident measurements are
30   made, while also allowing for a more robust retrieval of particle properties such as spectral single-scattering albedo.

# 1 Introduction

Among the geophysical quantities routinely produced from the NASA Earth Observing System's Multi-angle Imaging SpectroRadiometer (MISR) instrument are aerosol optical depth (AOD) and aerosol type. MISR measures upwelling short-wave radiance from Earth in four spectral bands centered at 446 (blue), 558 (green), 672 (red), and 866 nm (near-infrared, or NIR), at each of nine view angles spread out in the forward (f) and aft (a) directions along the flight path, at 70.5˚, 60.0˚, 45.6˚, 26.1˚, and nadir [*Diner et al.*, 1998]. The three near-nadir cameras are designated "Af," "Aa," and "An," and successively steeper-viewing pairs are "B," "C," and "D" cameras. MISR's multi-angle, multi-spectral radiance data sample air-mass-factors ranging systematically from one to three, making AOD retrieval possible even over bright desert surfaces, and improving retrieval sensitivity at low AOD compared to single-view instruments. In low-AOD situations, which are common over ocean, poor representation of the surface reflectance can limit aerosol retrieval accuracy, as the relative contribution of ocean under-light can be large, especially at shorter wavelengths. Therefore, applying a physical retrieval to constrain the ocean surface reflectance, of interest in itself as an indicator of ocean biological activity and its impact on the global carbon cycle (e.g., Behrenfeld et al., 2006), should also reduce the uncertainties in the concomitant aerosol retrievals, assuming that the aerosol and ocean signals do not co-vary substantially over MISR's 36 channels.

A second factor directly affecting the quality of almost every MISR geophysical data product is the accuracy of the instrument's radiometric calibration. As the MISR data record now exceeds 17 years of near-global coverage about once per week, the advantages of further refining the MISR calibration have increased multifold. This applies to determining AOD trends, and is especially true in the context of MISR's unique ability to retrieve aerosol type (Kahn and Gaitley, 2015). In addition to AOD and aerosol type, retrievals of ocean bio-optical properties from space are extremely sensitive to the calibration of the instrument, because only 5 to 20% of the top-of-atmosphere (TOA) reflected signal in the blue and green spectral bands, where ocean color is retrieved, arises from scattering related to ocean under-light (e.g., Figure 2; more generally, Gordon and Wang, 1994). We find that not only the absolute radiometric calibration, but also the MISR blue/green ratio, critical for ocean color applications, has changed over time.

This paper is organized as follows: section 2 reviews the datasets used in our analysis and the methodology adopted, section 3 presents the *Chl* retrievals and initial validation of the results, example retrievals are shown in section 4, and conclusions are given in section 5. MISR radiometric calibration corrections, including details of the observed temporal trends, are described in Appendix A.

# 2 Comparison datasets and methodology

## 2.1 The MISR Research Algorithm (RA)

The aerosol/*Chl* retrieval algorithm is summarized as a flow chart in Figure 1. An in-depth description of the main RA components can be found in Limbacher and Kahn (2014; 2015). Briefly, the algorithm finds the set of aerosol optical

models, associated aerosol amounts, and *Chl* values, that minimize the difference between the observed TOA reflectances (identical to BRFs described in Appendix A, but without the solar-zenith-angle normalization) and simulated values that are stored in a look-up table (LUT). The overall aim is to derive AOD and *Chl* over 1.1 km retrieval regions, conditioned on aerosol-type mixtures that produce TOA reflectances that meet certain $\chi^2$ criteria. In the current study, we compare the MISR RA *Chl* retrievals to coincident validation data taken at the surface, after all MISR calibration corrections are applied (Appendix A), and also identify the impact the refined ocean surface model has on the retrieved aerosol results for a few scenes, in Section 4 below.

## 2.2 MISR RA Enhanced Ocean Reflectance Model

Prior to Limbacher and Kahn (2014), the MISR RA simulated ocean surface was modeled as an isotropic (wind-speed-dependent only) Fresnel-reflector (Cox-Munk), with whitecap reflectance included. In Limbacher and Kahn (2014), we made adjustments to the whitecap reflectance, and added an ocean under-light term that includes molecular and particulate attenuation. In Limbacher and Kahn (2014, 2015), we used wind and ocean-color constraints from the Cross-Calibrated Multi-Platform (CCMP; Atlas et al., 2011) and GlobColour (Barrot et al., 2014) products (and a climatology where these products were unavailable), respectively, to prescribe the ocean's color.

For the current analysis, we continue using CCMP data for 10-meter wind speed (where available, otherwise we use the MISR Standard Algorithm (SA) wind data, which comes from monthly averaged values of QuikSCAT and SSMI (Michael Garay, personal communication). We set the surface pressure to 1013.25 mb, as we find a number of cases where the MISR Standard Product surface pressure over ocean is aliased from nearby mountains. This results from the different footprint sizes of the SA vs. the RA; the SA has a 17.6 km footprint, whereas the RA has a 1.1 km footprint. Additionally, instead of prescribing *Chl*, we now retrieve it directly in the algorithm by inverting our ocean color model. To do this, we use all four MISR spectral bands to simultaneously retrieve aerosol and *Chl*, with equal weighting, whereas the SA (Martonchik et al., 2009) and past versions of the RA retrieved only aerosol amount and type, and used only the red and NIR bands, where the ocean surface is darkest, except at high AOD. However, empiricalcamera weighting is applied to mitigate the effects of sun glint, and different uncertainties are assigned to the 36 MISR channels when evaluating the $\chi^2$ acceptance criteria, as discussed below.

Colored dissolved organic matter (CDOM) absorption is assumed to co-vary with *Chl* (Morel and Gentili, 2009). Relationships connecting *Chl* to absorption and back-scattering coefficients can be found in many places; the ones we used (Chen et al., 2003; Devred et al., 2006; Morel and Prieur, 1977; Morel 1988) are summarized in Sayer et al., (2010). For our ocean under-light model, we modify the absorption of light by seawater for the blue spectral band from the Morel and Prieur (1977), which was used previously in the RA, to more recent results from Lee et al., (2015).

The following equation gives a bidirectional water-leaving radiance:

$$L_w^+(\mu_0, \mu, \Delta\phi, \lambda, WS, \tau, mix, Chl) = E_d(\mu_0, \lambda, \tau, mix) * \Re(\mu, WS) * \left(\frac{b_b(\lambda, Chl)}{a(\lambda, Chl)}\right) * \frac{f}{Q}(\mu_0, \mu, \Delta\phi, \lambda, Chl) \qquad (1)$$

The following explanation of the terms in equation (1) is basically a summary of Morel et al. (2002), which is also where the LUT for f/Q and $\Re$ was obtained. Variable dependences are included here only if they are given in the Morel et al. (2002) LUT.

- $L_w^+$ represents the water-leaving radiance, which is the upward-directed radiance just above the water surface (excluding sun-glint). It is a function of the cosine of the solar zenith angle ($\mu_0$), the cosine of the view (camera) zenith angle ($\mu$), the relative azimuth between the sun and the sensor ($\Delta\phi$), the wavelength ($\lambda$), the wind speed ($WS$), the total column optical depth ($\tau$), aerosol optical model ($mix$), and Chlorophyll-a concentration ($Chl$).
- $E_d$ represents the downward directed solar irradiance at the bottom of the atmosphere.
- $\Re$ is a reflectance factor, the product of two effects: the fraction of the downward directed bottom-of-atmosphere irradiance ($E_d$) transmitted through the air-sea interface, and the fraction of the upward directed radiance from just beneath the air-sea interface transmitted through the interface.
- $b_b$ represents the total backscattering coefficient of the water plus other material within the water.
- $a$ represents the total absorption coefficient of the water plus the other material within the water.
- $f$ represents an empirical correction to the ratio of the backscattering to absorption (essentially a modification to the upward directed under-light irradiance).
- $Q$ represents the ratio of the upward-directed irradiance to radiance just below the air-sea interface. This term (along with $f$) is responsible for creating the directional dependence of the under-light on solar and viewing geometry.

$L_w^+$ is multiplied by the transmittance from the bottom of atmosphere to the camera ($T_{a,up)}$ to get the surface contribution to the TOA reflectances. Because the integrated water-leaving radiance, $L_w^+ << E_d$ (i.e., the under-light albedo is small), the probability that a photon will be multiply reflected due to under-light is very small, regardless of atmospheric loading, and is ignored, given other, larger uncertainties in the algorithm. However, multiple surface reflections due to sun-glint and whitecaps are directly accounted for in the radiative transfer code.

As we aim to extract both surface and aerosol information from the MISR data, we apply new camera weights when calculating the $\chi^2$ test variables used to assess the agreement between the observed reflectances and those derived for various aerosol component and mixture options. In the SA and previous versions of the RA, a glitter mask was applied arbitrarily to all cameras viewing within 40° of the specular direction. Instead, we now use a combination of glitter-angle and Rayleigh

NIR reflectance, calculated assuming $Chl$ = 0.1 mg/m$^3$ to assess glint-contamination in each camera. The new camera weights are the product of the following two empirically derived equations:

$$\rho_{weight,i} = 1.0 - min\left\{max\left[\frac{(\mu_i * \rho_{model,i}^{NIR} - 0.0075)}{0.0125 - 0.0075}, 0.0\right], 1.0\right\}, \tag{2}$$

$$glitter_{weight,i} = min\left\{max\left[\frac{(G_i - 25.0)}{40.0 - 25.0}, 0.0\right], 1.0\right\} \tag{3}$$

Here $\rho_{model}^{NIR}$ represents the modeled NIR Rayleigh reflectance over an ocean surface for a particular MISR camera ($i$), and $G$ is the glitter angle relative to the same MISR camera. The minimum and maximum reflectances were taken via forward modeling, and 25° was set as the minimum because as glitter angle decreases, a small error in wind speed could substantially impact the retrieval. Equation 2 returns a value of unity if the modeled NIR reflectance is ≤0.0075; this weight decreases linearly to zero if the modeled reflectance is ≥0.0125. Essentially, as the modeled glint strength increases, camera weighting decreases. Similarly, Equation 3 produces a value of unity if the glitter angle ≥40˚, decreasing linearly to zero for G ≤ 25˚. The product of these weights provides better glint masking than using an arbitrary cutoff, and the quality of these new weights should improve with the quality of the input wind speed data. Further, as we improve our ability to determine if a camera is glint-contaminated in the future, we will likely lower this minimum glitter-angle threshold.

Figure 2 illustrates the impact of including under-light in the MISR RA, for the blue and green-band retrieval TOA reflectance results. For this figure, MISR aerosol retrievals over dark water were performed using the multi-angular data for the NIR band only, because the ocean surface tends to be darkest at this wavelength (i.e., where under-light makes its smallest spectral contribution). When the retrieved aerosol properties are used in the forward radiative transfer model to simulate the MISR top-of-atmosphere (TOA) reflectances in the blue and green bands, but under-light is not included, there are large discrepancies in the modeled TOA reflectances compared to the original MISR observations (Figure 2, top two panels). However, when under-light is accounted for in the simulations (in this illustration using coincident MODIS Terra $Chl$ as input), the biases are substantially reduced, as shown in the lower two panels of Figure 2. As the MODIS-constrained $Chl$ was included when the aerosol retrieval was performed (using only the multi-angle NIR data), this example demonstrates the magnitude of the surface contribution to the TOA reflectances in the blue and green spectral bands. If surface contributions are not explicitly included, the aerosol retrievals would be skewed, and the spectral dependence of the anomaly could impact the derived aerosol type (e.g., Kahn and Gaitley, 2015), especially when the blue or green bands are included in the aerosol retrieval. In Section 4 we demonstrate the use of MISR to constrain $Chl$ self-consistently with the retrieval of aerosol over ocean.

## 2.2 MODIS Terra top-of-atmosphere reflectances

The MODIS TOA reflectances are key to several radiometric calibration adjustments detailed in Appendix A. As in Limbacher and Kahn (2014), MODIS-Terra equivalent reflectance data are used as a baseline to compare against MISR, especially for the nadir camera. We use the latest MODIS collection 6 TOA reflectances (Sun et al., 2012) with additional

5 corrections implemented via an algorithm provided by Alexi Lyapustin (Lyapustin et al., 2014; elaborated in Limbacher and Kahn, 2015). Primarily, we are interested in the following MODIS bands: 9 (443 nm, as compared to MISR's 446 nm blue), 4 (555 nm, as compared to MISR's 558 nm green), an average of bands 13 and 14 (effectively 672 nm, as compared to MISR's 672 nm red), and 2 (856 nm, as compared to MISR's 866 nm NIR). In the current study, MODIS reflectances are used only to remove flat-fielding artifacts in the MISR imagery and to make modifications to the ghosting parameterization

10 described in Limbacher and Kahn (2015), so the absolute calibration accuracy of MODIS is not critical here. The most critical assumptions are that MODIS swath-edge and scan-angle issues are minimal for the scenes of interest, and that pixel-to-pixel relative precision is high. Fortunately, because the MISR swath samples about 380 km around the center of the 2,300 km MODIS swath, the effects of MODIS swath-edge and scan-angle artifacts on the coincident data are minimal.

## 2.3 The SeaWiFS Bio-optical Archive and Storage System (SeaBASS) data set

15 The SeaBASS dataset (Werdell et al., 2002; https://seabass.gsfc.nasa.gov) was originally developed to compare products retrieved from sensors such as the Sea-viewing Wide Field-of-view Sensor (SeaWiFS) and MODIS with in situ bio-optical observations. We use SeaBASS chlorophyll validation data generated either by fluorometry or by high-performance liquid chromatography (HPLC). Uncertainties for HPLC and fluorometry *Chl* measurements are 5% and 8%, respectively (Heukelem et al., 2002). If HPLC (*Chl*) and fluorometry (*Chl*) data were acquired at the same location and time, we use the

20 HPLC (*Chl*) data; otherwise we use the fluorometry data. Because the MISR Standard Algorithm does not retrieve *Chl*, the MISR-SeaBASS coincidences were found by locating MODIS-Terra validation matchups (Bailey and Werdell, 2006) and setting the viewing-zenith angle maximum to 16°, which corresponds to the edge of the MISR nadir (AN) camera field-of-view. To assure meaningful SeaBASS observations for MISR *Chl* validation purposes, we also applied the following criteria: (1) minimum sea floor depth was set to 30 meters to mitigate errors due to sea floor reflections, especially in the

25 blue band, (2) maximum wind speed was set to 7 m/s to avoid whitecaps (eliminating ~25% of data), (3) maximum solar zenith angle was set to 70° to eliminate steep-incidence-angle effects, (4) maximum coefficient of variation for MODIS *Chl* was set to 0.15 to avoid aliasing due to spatial variability of the scene, (5) maximum SeaBASS-MISR time difference was set to 3 hours, and (6) minimum number of valid MODIS pixels was set to 25%. This produced 75 coincidences that have valid MISR aerosol/*Chl* retrievals. Of these 75 coincidences, 49 correspond to *Chl* < 1.5 (the *Chl* regime where the MISR

30 retrievals are expected to show good performance) and also have at least one valid MISR RA retrieval in a 5.5 x 5.5 km area surrounding the SeaBASS station passing our quality tests.

**2.4 MODIS Terra Chlorophyll-a**

Although we validate our *Chl* retrieval against the SeaBASS dataset for *Chl* <1.5, we also cross-compare our *Chl* results with those from MODIS-Terra (OBPG, OB.DAAC; 2014) to increase the number of coincidences (especially needed for *Chl* < 1.5), and because MISR and MODIS share a common platform. This ensures that the solar geometry is the same for MODIS and MISR, and minimizes potential collocation errors. To do this, we compare MISR RA-retrieved *Chl* with the corresponding MODIS Terra retrieved values (Hu et al., 2012). Details of the algorithm used to generate the MODIS data can be found at http://oceancolor.gsfc.nasa.gov/cms/atbd/chlor_a. Briefly, a training dataset containing collocated *in situ Chl* and spectral water leaving radiance ($L_w^+$) is used to empirically relate the ratio of blue-to-green MODIS $L_w^+$ to near-surface *Chl* (Werdell and Bailey, 2005). This same relationship is then used to retrieve MODIS *Chl* elsewhere, although the quality of the result also depends in part on the quality of the associated atmospheric correction (e.g., Kahn et al., 2016).

**2.5 The AErosol Robotic Network (AERONET)**

Although the main purpose of this paper is to demonstrate and validate our *Chl* retrieval, we also compare the new algorithm against AErosol RObotic NETwork (AERONET) observations for a few selected scenes. AERONET sun photometers (Holben et al., 1998) provide very accurate measurements of AOD (Eck et al., 1999) and Ångström exponent (ANG). The almucantar inversions (Dubovik and King, 2000) can provide constraints on particle sphericity (Dubovik et al., 2006; which we convert to fraction mid-visible AOD assigned to non-spherical particles, or Fr. Non-sph), and aerosol single scattering albedo (SSA), provided the aerosol loading is high (AOD at 440 nm > 0.4), the scattering angle range for the inversions is large, and the aerosol is relatively uniform over the range of view angles used for the inversion (Holben et al., AERONET's Version 2.0 quality assurance criteria).

# 3 Validation of MISR RA *Chl* retrievals against SeaBASS, and comparisons with MODIS

Collocation of the MISR and SeaBASS observations is of course critical to achieving meaningful comparisons. So for each SeaBASS-MISR coincidence, the corresponding location within a MISR orbit is identified as a block (180 blocks per orbit), line (128 along-track lines per block), and sample (512 across-track samples per block) at 1.1 × 1.1 km. We run the RA, as described in section 2.1, over three blocks of data per coincidence, centered on the MISR block that contains the MISR-SeaBASS coincidence. We then interpolate the MODIS-Terra *Chl* data, as well as the associated MODIS flags, to the MISR grid via nearest-neighbor interpolation. In an attempt to ensure the highest quality retrieval possible, we flag all MISR/MODIS data based on the following criteria:

- Any MISR/MODIS data where the MODIS *Chl* flag data is masked (at level 3) according to https://oceancolor.gsfc.nasa.gov/atbd/ocl2flags/.

- Any MISR/MODIS data where the MISR aerosol retrieval acceptance criterion is violated. In this case the criterion, $\chi^2 > 1.0$, is calculated over the all four wavelengths for all glint-free cameras (see section 2.1 above). This should help prevent poor aerosol retrievals impacting the MISR *Chl* retrieval.

- Any MISR/MODIS data where MISR 446nm AOD > 1.0. AOD above this value over ocean tends to occur only in cases of dust, smoke, or pollution plumes, or unmasked clouds. As the surface signal is very small for these cases, especially for the off-nadir cameras, MISR should have little or no sensitivity to *Chl* in these situations.

- Any MISR/MODIS data where the MISR *Chl* $\chi^2 > 1.0$, calculated over the over the blue and green "A" and "B" glint-free cameras, as these cameras contain the most information about the surface.

- Any MISR/MODIS data where *in situ Chl* > 10 mg m$^{-3}$, as our *Chl* model is not expected to work at all in this regime.

For comparisons with SeaBASS, we average (in $\log_{10}$ space) up to 5×5 MISR 1.1 km /MODIS 1 km *Chl* retrievals centered on the SeaBASS location, and compare each of the MISR and MODIS-Terra *Chl* to the corresponding SeaBASS value. Following conventional practice, $\log_{10}$ of the MISR, MODIS, and SeaBASS *Chl* data is taken before any statistics are computed, except the mean relative error (MRE).

## 3.1 Validation against SeaBASS

Figure 3 shows scatterplots for MISR and MODIS-Terra retrieved *Chl* vs. SeaBASS coincident *in situ Chl*. Points left of the black vertical line in Figure 3 and Table 1 demonstrate MISR sensitivity to retrieving Chlorophyll-a when the *in situ* value is less than 1.5 mg m$^{-3}$, which represents an upper bound on where we expect good-quality results. Statistics for $Chl_{in\ situ} \leq 10$ in Table 1 are shown for completeness. Compared to SeaBASS, for *in situ Chl* values $\leq 1.5$ mg m$^{-3}$, MISR reports a correlation coefficient (r) of 0.86, a median absolute error (MAE) of 0.10, root-mean-squared error (RMSE) of 0.25, and MRE of 0.52. We also performed three sets of the two-sample Kolmogorov-Smirnov test to compare whether these MISR, MODIS, and SeaBASS populations are distinguishable. The null hypothesis that the MISR and MODIS datasets are taken from the same distribution cannot be rejected (p=0.96), likely a result of having too few data points and/or strong co-variance. Not surprisingly, statistics for the 49 SeaBASS coincidences that meet our criteria indicate that the MISR RA performs almost as well as MODIS Terra for these cases. P-values of 0.25 and 0.37 also indicate that although the MISR and MODIS *Chl* data (respectively) are not statistically distinguishable from SeaBASS, they appear more similar to each other than they are to SeaBASS. Given the small sample size, it is not possible to draw strong conclusions about whether MISR could in general add value to the MODIS Terra Ocean color product in regions where MODIS-Terra reports *Chl*, despite the likelihood that MISR aerosol retrieval constraints would produce a more accurate atmospheric correction. However, MISR can add value in the glint-contaminated portion of the MODIS-Terra orbit, and probably in regions of medium-high aerosol loading (both of which are shown subsequently), where aerosol-type information could improve surface retrieval results (e.g., *Kahn et al.*, 2016).

### 3.2 Comparison against MODIS-Terra

Because the SeaBASS validation dataset contains very few matchups with MISR, in part due to the relatively narrow MISR swath, we compare MISR 1.1 km *Chl* retrievals with collocated MODIS 1 km *Chl* retrievals over much larger regions surrounding the MISR-SeaBASS coincidence locations, using the method described above.  We compare to MODIS-Terra for this regional-context exercise due to the assessments already performed on the MODIS *Chl* data with the much larger number of MODIS-SeaBASS coincidences (e.g., *Franz et al.*, 2012). As such, we compare the MISR RA *Chl* data with all valid pixels for which MODIS *Chl* $\leq$ 10 mg m$^{-3}$.

Figure 4 shows comparisons between the MISR RA and MODIS-retrieved *Chl*, for MODIS *Chl* $\leq$10.0 mg m$^{-3}$. The black vertical line indicates 1.5 mg m$^{-3}$, as we expect higher-quality MISR *Chl* retrievals to the left of this line.  The agreement between MISR and MODIS is best below MISR-retrieved *Chl* values of 0.5 mg m$^{-3}$.  For MISR *Chl* between 0.5 and 3.0 mg m$^{-3}$, Figure 4 indicates that a scale factor could be applied to the MISR data to bring the data into better agreement with MODIS (and likely SeaBASS as well).  Statistics for the MISR-MODIS *Chl* comparisons, as a function of MODIS-retrieved *Chl*, are summarized in Table 2.  Comparing MISR vs. MODIS for the ~1.5 million data points with MODIS *Chl*<1.5 mg m$^{-3}$: r=0.96, MAE=0.09, RMSE=0.15, and MRE=0.23.  A two-sample Kolmogorov-Smirnov test comparing these two datasets demonstrates that they are statistically different (p<<0.001).  Overall, although Figure 4 and Table 2 indicate that the agreement between MISR and MODIS appears to be much better than the agreement between either MISR or MODIS and SeaBASS (Figure 3 and Table 1), it is possible that this is an artifact of a small MISR-SeaBASS sample size. However, comparisons between MODIS-Terra, SeaWIFS, and SeaBASS on the SeaBASS website suggest that this behavior is real, as SeaWIFS and MODIS-Terra agree much better with each other than with SeaBASS (https://seabass.gsfc.nasa.gov/search#bio). This strongly suggests that satellite remote-sensing co-variation is playing a substantial role in the comparisons between MISR, MODIS and SeaBASS.  Interestingly, SeaWIFS also agrees better with MODIS-Terra than MISR does.  Regardless, Figures 3 and 4 indicate that there is skill in the MISR Chl retrieval, which could be exploited.

## 4. Example MISR Aerosol-Surface Retrievals Over Ocean

We present here two examples of individual MISR RA joint surface and atmosphere retrievals, and comparisons with the corresponding MISR SA retrievals, MODIS *Chl* results, and embedded AERONET AOD measurements and particle property retrievals.  Figure 5 presents both the SA and RA aerosol retrievals, along with the MISR RA and MODIS *Chl* results for a region of the Atlantic along the east coast of the US that includes the Chesapeake Bay and two coastal AERONET sties, in August 2003.  Weakly to non-absorbing, relatively small, pollution particles are expected in this region and season, as confirmed by the AERONET inversion results.  Both the SA (Diner et al., 2008; Kahn et al., 2010) and RA also identify the scene as dominated by small, spherical particles.  Although the

RA finds weakly or non-absorbing particles spread fairly uniformly over the entire scene, the SA appears to incorrectly identify part of the scene as contaminated by moderately absorbing aerosol. The MISR SA best estimate aerosol mixture preferentially selects lower SSA (Figure 5, ~0.91) aerosol mixtures near the coast, where both MODIS and the MISR RA report elevated *Chl*. In this same region, AERONET and MISR RA find that SSA falls within the range of 0.98 to 1.0.  For particle size, represented here by ANG, the MISR RA tends to pick slightly larger aerosol models (ANG~1.72), in poorer agreement with AERONET (ANG~2.05) than the SA (ANG~2.00).  This is probably related to the aerosol optical model options in the RA (e.g., Limbacher and Kahn, 2014), which are being reconsidered as part of continuing work.  Ultimately, we are hoping to systematically acquire direct, *in situ* measurements of the particle optical and chemical properties for the major aerosol air mass types, to put these remote-sensing algorithm assumptions on more solid footing [*Kahn et al.*, 2016].  Note also that the MISR *Chl* results compare very well with the corresponding MODIS values where coincident retrievals were obtained, and here the multi-angle data offer an advantage, as the MODIS camera is in sun-glint over the eastern half of the scene, whereas the MISR off-nadir cameras make it possible to perform *Chl* and aerosol retrievals over the entire area.

Figure 6 captures a scene in the mid-south Atlantic Ocean near Ascension Island, where smoke advected from southern Africa is commonly found. Both the SA and RA identify much of the scene as dominated by small, spherical absorbing aerosol, consistent with both the Ascension Island AERONET station and expectation.  The scene is covered in broken cloud, typical of much of this ocean region, which makes aerosol remote-sensing retrievals especially challenging.  Both the SA and the RA results exhibit 3-d light-scattering effects near cloud edges.  Here difference between the SA and RA retrieval-region sizes has significant consequences: the SA appears to have more coverage, whereas the cloud-edge anomalies are more localized in the higher-resolution RA retrievals, and the SA shows substantially more SSA (and hence retrieved aerosol type) variability ($0.92 \pm 0.08$) compared to the RA ($0.91 \pm 0.04$).  The variability artifacts due to 3-d effects also show up in the ANG and Fr. Non-Sph for both the SA and RA, and are reflected in the MISR RA retrieved *Chl*, giving an indication of the impact aerosol type has on retrieved ocean color.

## 5. Conclusions

In Limbacher and Kahn (2014), we detailed extensive modifications to the MISR Research Aerosol retrieval algorithm (RA) that reduced the 0.024 AOD high bias for $AOD_{558nm} < 0.10$ to ~0.01 or less.  The modifications also improved the results of the RA in general, compared to a set of about 1,100 ground-truth observations from coincident AERONET sun photometer observations.  We also found that the success of MISR aerosol retrieval algorithm refinements depends in part on the

accuracy of instrument radiometric calibration. So, in Limbacher and Kahn (2015), we implemented a stray-light correction for the near-nadir cameras based on empirical image analysis with MODIS. This further reduced the remaining high bias at low AOD and also improved statistical comparisons to the validation data overall. Here, we introduce a coupled surface component to the RA over water. More accurately accounting for ocean surface contributions to TOA reflectance should
5    improve aerosol-type retrievals (which will be explored in part II of this paper). As part of the MISR calibration refinement effort, we also performed a radiometric trend analysis over three stable, relatively homogeneous desert sites to identify and quantify temporal radiometric drift in each of the 36 MISR channels.

Validation of the MISR RA-retrieved *Chl,* with all radiometric corrections applied, was performed in part by comparison
10   with coincident SeaBASS *in situ* observations. Further comparisons were made against the previously validated MODIS-Terra ocean color *Chl* retrievals, because of the relatively small MISR-SeaBASS coincident dataset. Results show that the MISR RA can retrieve *Chl* reliably if the MODIS-reported $Chl \leq 1.5$ mg m$^{-3}$, which represents a large fraction of the Earth's ocean area (Figure 4). Compared to SeaBASS, for *in situ Chl* values $\leq 1.5$ mg m$^{-3}$, MISR reports a correlation coefficient of 0.86, MAE is 0.10, RMSE is 0.25, and MRE is 0.52. A comparison of the 49 coincident MISR, MODIS, and SeaBASS *Chl*
15   observations (Figure 3), using three two-sample Kolmogorov-Smirnov tests, indicates that it is not possible to distinguish statistically between any of these three small *Chl* data sets. For the larger (n=1,499,610) MISR-MODIS dataset with MODIS-retrieved $Chl \leq 1.5$ mg m$^{-3}$, we find r=0.96, MAE=0.09, RMSE=0.15, and MRE=0.23. Although the MISR RA as implemented here lacks much sensitivity to retrieved *Chl* above 1.5 mg m$^{-3}$, and especially above about 3 mg m$^{-3}$, this result was anticipated, due to the lack of spectral bands between 446 and 558 nm (Diner et al, 1998). However, with further work,
20   adjustments to the scattering and absorption terms in Equation (1) might improve the results in the higher *Chl* regime, particularly if MODIS-Terra reflectances can be integrated into the algorithm.
Obtaining MISR *Chl* retrievals can help fill in the glint-contaminated regions in the single-view MODIS-Terra swath near the solar equator, as only a few of MISR's nine view angles will be contaminated by glint in any one location, allowing the others to be used for the aerosol/*Chl* retrieval. In addition, these MISR *Chl* results are derived self-consistently with aerosol
25   amount and type in a physical retrieval, which from the ocean color perspective provides a more robust "atmospheric correction" for the surface retrieval. This work formally opens the door for the use of MISR data in ocean color, complementing the better-constrained and more extensive spectral coverage of MODIS ocean color retrievals. With the improved ocean-surface boundary condition, the MISR multi-angular data should also allow for better-constrained aerosol products, particularly non-sphericity and single-scattering albedo. In the future, it might be possible to ingest collocated
30   MISR and MODIS-Terra reflectances, and use the strengths of each instrument in a complimentary manner.

**Acknowledgments**

We thank Chris Proctor and NASA's Ocean Biology Processing Group for providing the MODIS Terra Ocean Color products and the SeaBASS group (and cruise PIs) for compiling and providing their in situ ocean color data sets. We thank our colleagues on the Jet Propulsion Laboratory's MISR instrument team and at the NASA Langley Research Center's Atmospheric Sciences Data Center for their roles in producing the MISR Standard data sets, and Brent Holben at NASA Goddard and the AERONET team for producing and maintaining this critical validation dataset.  We also thank Carol Bruegge, Sergey Korkin and Andrew Sayer for *many* helpful discussions, Alexei Lyapustin for providing MODIS code, as well as Andrew Sayer, James Butler, and Carol Bruegge for comments on an early version of the manuscript.  This research is supported in part by NASA's Climate and Radiation Research and Analysis Program under H. Maring, and NASA's Atmospheric Composition Program under R. Eckman.

## Appendix A. MISR Radiometric Calibration Adjustments

As mentioned in the introduction, instrument calibration can affect retrieval products such as AOD, aerosol type, and ocean surface properties (Limbacher and Kahn, 2015). Calibration includes determination of (1) the absolute radiometric scale, as well as (2) the relative band-to-band response among the four MISR spectral bands, (3) camera-to-camera response among the nine MISR cameras, (4) flat-fielding across the MISR imagery (i.e., CCD detector-based gain errors, which show up as across-track biases in reflectance), and (5) temporal trends in these quantities.  Considerable effort has been expended to assess MISR radiometric calibration and to meet the standards of approximately 3% absolute and 1% channel-to-channel, established pre-launch.  Previous work involved pre-launch laboratory studies (Bruegge et al., 1999), on-board-calibrator analysis and lunar calibration, along with vicarious calibration over bright land targets (Bruegge et al., 2004; 2007; 2014), symmetry tests comparing the forward and aft-viewing cameras across the solar equator (Diner et al., 2004), and over-ocean dark target vicarious calibration (Kahn et al., 2005). Cross-calibration analysis has been performed over bright and dark land and ocean surfaces with the MODerate-resolution Imaging Spectroradiometer (MODIS), that flies aboard the Terra satellite with MISR (Lyapustin et al., 2007), and MODIS combined with the MEdium Resolution Imaging Spectrometer (MERIS), the airborne AirMISR instrument, the LandSat-7 ETM+ (Bruegge et al., 2007), and the Polarization and Directionality of the Earth's Reflectances-2 (POLDER-2) (Lallart et al., 2008).  A synthesis of much of this work is given in Bruegge et al. (2014).  Limbacher and Kahn (2015) used image analysis, including comparisons with coincident MODIS observations, to characterize flat-fielding errors, and to identify empirical relationships that correct anomalies exhibiting spatial structure in high-contrast scenes, an aggregate of "ghosting" light reflections (or stray-light) within the cameras.  Here we make minor adjustments to our earlier ghosting and flat-fielding corrections.  For the flat-fielding characterization, we select only low-contrast scenes, where ghosting artifacts are minimal, and we then normalize the mean MISR-MODIS ratios for the entire scene to unity.  For the ghosting modifications, we normalize the MISR-MODIS ratios to an area of little contrast, where

stray light is unlikely to be an issue. In the course of that analysis, we also observed systematic, temporal drifts in the measured reflectances, addressed in A.2 below.

## A.1. TOA Reflectance Pre-processing and Stray-light Corrections

In the RA pre-processing, all MISR L1B2 reflectance data are first averaged to 1.1 km. The reflectances are then rotated to the L1B1 format, as described in Limbacher and Kahn (2015), and updated stray-light and flat-fielding corrections are applied before being rotated back to L1B2 format. Compared to Limbacher and Kahn (2015), we modify the stray-light corrections in the following way:

- The primary ghost term has been divided into a discrete ghosting component (reflected images of features in the scene) and an unstructured veiling-light component.
  - o This revised primary ghost has a band-and-camera-dependent along-track offset applied, as indicated by MISR lunar observations acquired on 14 April 2003 (e.g., Bruegge et al., 2004).
  - o The primary ghost image is also stretched/squeezed across-track (for the near-nadir "A" cameras only), based on further comparisons with MODIS Terra, following the same approach as our earlier work.
- Via ray tracing, it was found that the "secondary ghosting" term in Limbacher and Kahn (2015) distributes light uniformly from the left- or right-most ~1/3 of the scene to the remainder of that half of the scene (Ab Davis, personal communication, 2016), and the correction has been modified accordingly.
- All stray-light terms are now represented as convolutions, which are much quicker to compute than applying the functions pixel-by-pixel as was done in our earlier work.
- The magnitudes of all stray-light terms have been adjusted as a result of adding the unstructured veiling-light component.
- The stray-light model for the An camera (all four bands) is used for all off-nadir cameras. Only the along-track offset and primary ghost stretching are varied by camera.

We then correct for temporal degradation in the MISR calibration (see A.2. below) and revise the band-to-band calibration. We change the band-to-band calibration by increasing the red reflectance 0.75% and decreasing the near-infrared (NIR) reflectance 0.75%, adjustments that are within the calibration uncertainty and are required to match a global set of coincident, spectral aerosol optical depth validation data (*Limbacher and Kahn,* 2014; 2015). We also apply corrections to the radiance data to smooth out apparent anomalies in the instrument gain, based on Bruegge et al. (in preparation).

## A.2. Temporal Trend Characterization and Correction

We characterize here temporal trends in the instrument calibration, again using an empirical image-analysis approach. Bruegge et al. (2014) identified temporal trends in the MISR bidirectional reflectance factor (BRF, computed as described in Step 1a. below) data, based on a time-series of mean BRFs for a region approximately 10 × 20 high-resolution (275 m) MISR pixels, a region roughly 2.5 × 6 km in size, centered at (27.21˚ N; 26.10˚ E) within the Egypt-1 desert site. Although

5  this site is stable over time, we adopt a different methodology, similar to Lyapustin et al. (2014), but without performing an atmospheric correction (thus we assume no trend in TOA reflectance due to changes in AOD/aerosol type). The temporal trending analysis is done here based on BRFs averaged over larger areas, and at three stable desert sites (Egypt-1, Libya-1, and Libya-4). Compared to Bruegge et al. (2014), both techniques are valid, but we limit geo-location error by averaging, and we reduce the influence of clouds by selecting the median BRF pixel from each case.

10  The first challenge to performing the temporal-trend analysis is finding suitable homogeneous regions. The following was done to select study regions within each of the three sites: the spectral coefficients of variation (standard deviation divided by the mean) were calculated for rolling 50 × 50 pixel patches, in each spectral band of the nadir camera, for three or more orbits, and (b) the 50 × 50 pixel patch having the smallest maximum coefficient of variation among all four bands was chosen for subsequent time-series analysis. The central coordinates for the sites selected are: Egypt-1 (26.62° N, 26.18° E),

15  Libya-1 (24.73° N, 13.52° E), and Libya-4 (28.77° N, 23.50° E). Information about these calibration sites can be found at http://calval.cr.usgs.gov/rst-resources/sites_catalog/radiometric-sites/test-site-gallery/.

The central coordinate of each study site is imaged repeatedly by MISR along at least two distinct paths having different sub-spacecraft ground tracks, and therefore different viewing geometries at the site. (A "path" is one of 233 ground tracks that the Terra satellite covers, repeatedly, every 16 days.) So the following procedure was applied separately to each path and

20  camera (6 paths × 9 cameras), for data acquired between January 1, 2002, and December 31, 2014, giving 13 full years of MISR data. (Prior to January 1 2002, the spacecraft equator-crossing time was not yet stable, so solar geometry varied too much for this time-series analysis.) All observations of each site, about four per month, were initially included. Note that we also apply flat-fielding corrections to the nadir camera (Limbacher and Kahn, 2015), and additional corrections to the radiance data in all cameras to smooth the instrument gain temporal samples (Carol Bruegge, personal communication,

25  2016). We characterize the temporal trends as follows:

    **1) Calculate median patch reflectance for each orbit**

        a. Perform Earth-Sun and solar zenith normalization according to: BRF=L*([π × $D^2$] / [E(i) × cos(SZA)]), where L is the top-of-atmosphere radiance, D is the sun-Earth distance in AU, E(i) is the band-weighted

30             exo-atmospheric solar irradiance for band (i), and SZA is the solar zenith angle.

        b. Calculate the median (and mean) BRF and standard deviation over a region 25 km in radius surrounding the central latitude/longitude coordinate.

c. If the wavelength-maximized coefficient of variation is less than 0.02, save the median BRF for use in the time series, otherwise discard the data.

Median BRF values for at least 193 orbits, and up to 229 orbits, were retained for all 6 paths, 4 spectral bands, and 9 cameras at this step.

**2) Remove outliers for each path/site and spectral band**

    a. Arrange the saved median BRFs by acquisition date, fit a line to the values, and subtract the linear trend from the data (to be added back after outliers are removed and the data are deseasonalized).

    b. Aggregate the data by day-of-year (DOY) and smooth the sorted, de-trended BRFs using a 21-point (i.e., ±10 data point) rolling average. (The data are sufficiently dense that dividing each data point with the mean of 21 surrounding data points does not create significant artifacts in the time-series.) This removes the seasonality, but does not remove outliers from the data, therefore allowing us to identify them.

    c. Identify BRFs that fall outside 2σ from time series.

    d. Remove the identified outliers from the original data.

This step removed 3-14% of data outliers from each time-series.

**3) De-seasonalize the data for each site and spectral band**

    a. Fit a line to the original, time-ordered BRFs (for all 13 years), with outliers removed, and again linearly de-trend the data.

    b. Re-aggregate the data by DOY and divide the BRFs by their 21-point (±10 data point) rolling average.

    c. Rearrange the data by time and add back the linear trend from Step 3a.

Step 3 is illustrated in Figure A1 for the Libya-4 site.

**4) Normalize the data**

    a. Normalize the data so the time-series mean for each spectral band at each site is 1.0, which retains the linear trends in each time-series, but allows data from multiple sites and paths to be compared.

The result is 216 normalized time-series, one for each MISR camera and band, for each of two paths at three sites.

b. These time-series are then aggregated across all paths to produce 36-time series, one for each MISR channel (Figure A2).

The linear percent change per decade and its 95th percent confidence interval are then calculated for each channel, and the results are presented in Table 3 and Figure A3. The trends are all negative, as might be expected due to sensor degradation over time. They are smallest in the blue band for all but the forward-viewing 70.5˚ (Df) and 60.0˚ (Cf) cameras, smallest for the aft-viewing 70.5˚ (Da) and 60.0˚ (Ca) cameras for all bands except the NIR, and largest for the An, and 26.1˚ forward (Af) and aft-viewing (Aa) cameras. The largest drift overall is about -1.5% per decade for the An camera red and NIR bands, and the uncertainty in these results ranges from ~0.1 % per decade to ~0.4 % per decade, depending on wavelength

and camera. The apparent stability of the MISR blue band is probably due to the use of the blue diode to assess degradation of the MISR on-board calibration panels (Bruegge et al., 2007).  Because MISR calibration assumes that the panel degrades in a spectrally invariant way (likely a poor assumption), this subsequently results in a spectral variant TOA reflectance drift with time.

## References

Atlas, R., R. N. Hoffman, J. Ardizzone, S. M. Leidner, J. C. Jusem, D. K. Smith, D. Gombos, 2011. A cross-calibrated, multiplatform ocean surface wind velocity product for meteorological and oceanographic applications. Bull. Amer. Meteor. Soc., 92, 157-174. doi: 10.1175/2010BAMS2946.1

Bailey, S.W. and P.J. Werdell, 2006. A multi-sensor approach for the on-orbit validation of ocean color satellite data products, Rem. Sens. Environ. **102** , 12-23.

Barrot, G., Mangin, A., and Pinnock, S., 2010. GlobColour Product User Guide, http://www.globcolour.info, accessed: 31 January 2014.

Behrenfeld, M.J., R.T. O'Malley, D.A. Siegel, C.R. McClain, J.L. Sarmiento, G.C. Feldman, A.J. Milligan, P.G. Falkowski, R. M. Letelier, and E.S. Boss, 2006. Climate-driven trends in contemporary ocean productivity.  Nature 444, 752-755.

20  Bruegge, C.J., D.J. Diner, R.P. Korechoff, and M. Lee, 1999.  MISR Level 1 Radiance Scaling and Conditioning Algorithm Theoretical Basis. Jet Propulsion Laboratory JPL D-11507, Rev E. From: http://eospso.gsfc.nasa.gov/sites/default/files/atbd/atbd-misr-02.pdf

Bruegge, C.J., W.A. Abdou, D.J. Diner, B.J. Gaitley, M.C. Helmlinger, R.A. Kahn, and J.V. Martonchik, 2004. Validating
25  the MISR radiometric scale for the ocean aerosol science communities. In: Post-launch calibration of satellite sensors, Stanley A. Morain and Amelia M. Budge, editors. A.A. Balkema Publishers, Leiden, Netherlands, pp.103-115.

Bruegge, C.J., D.J. Diner, R.A. Kahn, N. Chrien, M.C. Helmlinger, B.J. Gaitley, W.A. Abdou, 2007. The MISR radiometric calibration process, Remt. Sensing Enviorn. 107, 2-11, doi:10.1016/j.rse.2006.07.024.

Bruegge, C.J., D.J. Diner, E. Gray, V. Jovanovic, E. Gray, L. Di Girolamo, and G. Zhao, 2014. Radiometric stability of the Multi-angle Imaging SpectroRadiometer (MISR) following 15 years on-orbit. Proc. SPIE V. 9218, doi: 10.1118/12.2062319.

Chrien, N. L., C. J. Bruegge, and B. J. Gaitley, 2001. AirMISR laboratory calibration and in-flight performance results. Remt. Sens. Environ. 77, 328-337.

5   Chen, C., P. Shi, and H. Zhan, 2003. A local algorithm for estimation of yellow substance (gelbstoff) in coastal waters from SeaWiFS data: Pearl River estuary, China, International Journal of Remote Sensing 24 (5), doi: 10.1080/0143116021000047901

Devred, E., S. Sathyendranath, V. Stuart, H. Maass, O. Ulloa, and T. Platt, 2006. A two-component model of phytoplankton
10  absorption in the open ocean: Theory and applications, J. Geophys. Res., 111, C03011, doi:10.1029/2005JC002880

Diner, D. J., et al., 1998. Multi-angle Imaging SpectroRadiometer (MISR) instrument description and experiment overview, in IEEE Transactions on Geoscience and Remote Sensing, vol. 36, no. 4, pp. 1072-1087, doi: 10.1109/36.700992

15  Diner, D.J., R.A. Kahn, C.J. Bruegge, J.V. Martonchik, W.A. Abdou, B.J. Gaitley, M.C. Helmlinger, O.V. Kalashnikova, and W-H. Li, 2004. Refinements to MISR's radiometric calibration and implications for establishing a climate-quality aerosol observing system. Proc. of SPIE Vol. 5652, 57-65.

Diner, D. J., et al. 2008. Multi–Angle Imaging SpectroRadiometer Level 2 Aerosol Retrieval Algorithm Theoretical Basis,
20  Revision G, JPL D–11400, Jet Propulsion Laboratory, California Institute of Technology, Pasadena.

Dubovik, O. and M. D. King, 2000: A flexible inversion algorithm for retrieval of aerosol optical properties from Sun and sky radiance measurements, J. Geophys. Res., 105, 20 673-20 696.

25  Dubovik, O., A. Sinyuk, T. Lapyonok, B. N. Holben, M. Mishchenko, P. Yang, T. F. Eck, H. Volten, O. Munoz, B. Veihelmann, W. J. van der Zande, J-F Leon, M. Sorokin, and I. Slutsker, 2006. Application of spheroid models to account for aerosol particle nonsphericity in remote sensing of desert dust. J. Geophys. Res., 111, doi:10.1029/2005JD006619

Eck, T. F., Holben, B. N., Reid, J. S., Dubovik, O., Smirnov,A., O'Neill, N. T., Slutsker, I., and Kinne, S., 1999. Wavelength
30  dependence of the optical depth of biomass burning, urban, and desert dust aerosols, J. Geophys. Res., 104, 31333–31349, doi:10.1029/1999JD900923.

Franz, B.A., S.W. Bailey, G. Meister, and P.J. Werdell, 2012. Consistency of the NASA Ocean Color Data Record. Proc. Ocean Optics 2012, Glasgow, Scotland, 8-12 October 2012.

Gordon, H.R. and Wang, M., 1994. Retrieval of water-leaving radiance and aerosol optical thickness over oceans with SeaWiFS: a preliminary algorithm. Appl. Opt. 33, 443–452.

Heukelem, L. V., Thomas, C. S., and P. M. Glibert, 2002. Sources Of Variability In Chlorophyll Analysis By Fluorometry And High Performance Liquid Chromatography In a SIMBIOS Inter-Calibration Exercise. NASA TM 2002-02338-0.

Holben, B. N., Eck, T. F., Slutsker, I., Tanre, D., Buis, J. P., Sezter, A., Vermote, E., Reagan, J. A., Kaufman, Y. J., Nakajima, T., Lavenu, F., Jankowiak, I., and Smirnov, A., 1998 AERONET – a federated instrument network and data archive for aerosol characterization, Remote Sens. Environ., 66, 1–16.

Holben, B. N. et al., AERONET's Version 2.0 quality assurance criteria. Accessed 8-26-2016. http://aeronet.gsfc.nasa.gov/new_web/Documents/AERONETcriteria_final1.pdf

Hu, C., Z. Lee, and B. Franz, 2012. Chlorophyll-a algorithms for oligotrophic oceans: A novel approach based on three-band reflectance difference, J. Geophys. Res., 117, C01011, doi:10.1029/2011JC007395.

Kahn, R., W-H. Li, J. Martonchik, C. Bruegge, D. Diner, B. Gaitley, W.Abdou, O. Dubovik, B. Holben, S. Smirnov, Z. Jin, and D. Clark, 2005. MISR low-light-level calibration, and implications for aerosol retrieval over dark water, J. Atmosph, Sci. 62, 1032-1062.

Kahn, R.A., B.J. Gaitley, M.J. Garay, D.J. Diner, T. Eck, A. Smirnov, and B.N. Holben, 2010. Multiangle Imaging SpectroRadiometer global aerosol product assessment by comparison with the Aerosol Robotic Network. J. Geophys. Res. 115, D23209, doi: 10.1029/2010JD014601.

Kahn, R. A., and B. J. Gaitley, 2015. An analysis of global aerosol type as retrieved by MISR. J. Geophys. Res. Atmos. 120, doi:10.1002/2015JD023322.

Kahn, R.A., A. M. Sayer, Z. Ahmad, and B. Franz, 2016. How Aerosol Amount and Type Affect SeaWiFS Ocean Color Retrievals. J. Atm. Ocean Tech. 33:6, 1185-1209, doi: 10.1175/JTECH-D-15-0121.1

Lallart, P., R.A. Kahn, and D. Tanré, 2008. POLDER2/ADEOSII, MISR, and MODIS/Terra reflectance comparisons, J. Geophys. Res., 113, D14S02, doi:10.1029/2007JD009656.

Lee, Z., J. Wei, K. Voss, M. Lewis, A. Bricaud, and Y. Huot, 2015. Hyperspectral absorption coefficient of "pure" seawater in the range of 350–550 nm inverted from remote sensing reflectance, Appl. Opt. 54, 546-558

Limbacher, J.A., and R.A. Kahn, 2014. MISR Research-Aerosol-Algorithm Refinements For Dark Water Retrievals. Atm. Meas. Tech. 7, 1-19, doi:10.5194/amt-7-1-2014.

Limbacher, J. A. and R.A. Kahn, 2015. MISR empirical stray light corrections in high-contrast scenes. Atm. Meas. Tech., 8, 2927-2943, doi:10.5194/amt-8-2927-2015.

Lyapustin, A., Y. Wang, R. Kahn, J. Xiong, A. Ignatov, R. Wolfe, A. Wu, B. Holben, C. Bruegge, 2007. Analysis of MODIS-MISR calibration differences using surface albedo around AERONET sites and cloud reflectance, Remt. Sensing Enviorn. 107, 12-21, doi:10.1016/j.rse.2006.09.028.

Lyapustin, A., Y. Wang, X. Xiong, G. Meister, S. Platnick, R. Levy, B. Franz, S. Korkin, T. Hilker, J. Tucker, F. Hall, P. Sellers, A. Wu, and A. Angal, 2014. Science impact of MODIS C5 calibration degradation and C6+ improvements. Atmos. Meas. Tech. Discuss., 7, 7281–7319.

Martonchik, J.V., R.A. Kahn, and D.J. Diner, 2009. Retrieval of Aerosol Properties over Land Using MISR Observations. In: Kokhanovsky, A., ed., Satellite Aerosol Remote Sensing Over Land. Springer, Berlin.

Morel, A. and L. Prieur, 1977. Analysis of variations in ocean color, J. Limnology and Oceanography, 22, 709–722

Morel, A., 1988. Optical modeling of the upper ocean in relation to its biogenous matter content (case I waters), J. Geophys. Res., 93(C9), 10749–10768, doi:10.1029/JC093iC09p10749.

Morel, A., Antoine, D. and B. Gentili, 2002. Bidirectional reflectance of oceanic waters: Accounting for Raman emission and varying particle phase function, Appied Optics, 41, 6289-6306

Morel, A. and B. Gentili, 2009. A simple band ratio technique to quantify the colored dissolved and detrital organic material from ocean color remotely sensed data, Remote Sensing of Environment, Volume 113, Issue 5, Pages 998-1011, ISSN 0034-4257, http://dx.doi.org/10.1016/j.rse.2009.01.008.

NASA Goddard Space Flight Center, Ocean Biology Distributed Active Archive Center, 2014. Moderate Resolution Imaging Spectroradiometer (MODIS)-Terra Ocean Color Data, NASA OB.DAAC, Greenbelt, MD, USA. Accessed 09/16/2016. Maintained by NASA Ocean Biology Distibuted Active Archive Center (OB.DAAC), Goddard Space Flight Center, Greenbelt MD.

NASA Goddard Space Flight Center, Ocean Ecology Laboratory, Ocean Biology Processing Group (OBPG), 2014. MODIS-Terra L2 chlor_a and l2_flags; NASA Goddard Space Flight Center, Ocean Ecology Laboratory, Ocean Biology Processing Group. Accessed on 09/16/2016.

Sayer, A. M., Thomas, G. E., and Grainger, R. G., 2010. A sea surface reflectance model for (A)ATSR, and application to aerosol retrievals, Atmos. Meas. Tech., 3, 813-838, doi:10.5194/amt-3-813-2010.

Sun, J., A. Angal, X-J. Xiong, H. Chen, X. Geng, A. Wu, T-J. Choi, and M. Chu, 2012. MODIS Reflective Solar Bands Calibration Improvements in Collection 6. Proc. of SPIE Vol. 8528, 85280N.

Werdell, P.J. and S.W. Bailey, 2002. The SeaWiFS Bio-optical Archive and Storage System (SeaBASS): Current architecture and implementation, NASA Tech. Memo. 2002-211617, G.S. Fargion and C.R. McClain, Eds., NASA Goddard Space Flight Center, Greenbelt MD, 45 pp.

Werdell, P.J. and S.W. Bailey, 2005. An improved in situ data set for bio-optical algorithm development and ocean color satellite validation, Rem. Sens. Environ. **98** , 122-140

**Table 1: Statistics of Chlorophyll-a retrievals as compared to SeaBASS**

| $Chl_{in\ situ}$ <1.5 | r | MAE | RMSE | Fr. Err | # |
|---|---|---|---|---|---|
| MISR RA | 0.86 | 0.10 | 0.25 | 0.52 | 49 |
| MODIS | 0.91 | 0.14 | 0.22 | 0.54 | 49 |
| MISR RA vs. MODIS | 0.92 | 0.10 | 0.19 | 0.33 | 49 |
| $Chl_{in\ situ}$<10.0 | r | MAE | RMSE | Fr. Err | # |
| MISR RA | 0.78 | 0.18 | 0.37 | 0.57 | 75 |
| MODIS | 0.88 | 0.16 | 0.26 | 0.52 | 75 |
| MISR RA vs. MODIS | 0.90 | 0.15 | 0.22 | 0.40 | 75 |

**In this table, r is the Pearson correlation coefficient, MAE is the median absolute error, RMSE is the root mean squared error between the satellite retrieval and in situ data, Fr. Err is the mean absolute fractional error of the retrieval with respect to the measurement, and # is the number of validation cases included. The last row for $Chl_{in\ situ}$ <1.5 and $Chl_{in\ situ}$ <1.5 represents the statistics of MISR vs. MODIS.**

**Table 2: Statistics of MISR vs. MODIS Regional Chlorophyll-a retrievals**

| MISR *Chl* $\chi^2$<1.0, MISR $\chi^2$<1.0 | r | MAE | RMSE | Fr. Err | # |
|---|---|---|---|---|---|
| MODIS *Chl* < 1.5 | 0.96 | 0.09 | 0.15 | 0.23 | 1499610 |
| MODIS *Chl* < 10 | 0.94 | 0.11 | 0.20 | 0.29 | 1829153 |

**In this table, r is the Pearson correlation coefficient, MAE is the median absolute error, RMSE is the root mean squared error between MISR and MODIS-Terra, Fr. Err is the mean absolute fractional error of the MISR RA retrieval with respect to MODIS-Terra, and # is the number of validation cases included.**

**Table 3**: Decadal trend values (in percent) aggregated over three stable desert sites for the 36 MISR channels

| Fit | Df | Cf | Bf | Af | An | Aa | Ba | Ca | Da |
|---|---|---|---|---|---|---|---|---|---|
| Blue | -1.03 | -1.22 | -0.85 | -1.14 | -0.22 | -0.44 | -0.68 | -0.37 | -0.20 |
| Green | -1.22 | -1.28 | -1.21 | -1.47 | -1.34 | -1.12 | -1.00 | -0.82 | -0.63 |
| Red | -1.13 | -1.20 | -1.22 | -1.42 | -1.51 | -1.24 | -1.08 | -0.95 | -0.80 |
| NIR | -1.15 | -1.24 | -1.29 | -1.46 | -1.49 | -1.43 | -1.29 | -1.22 | -1.16 |
| | | | | | | | | | |
| **95% CI Fit** | Df | Cf | Bf | Af | An | Aa | Ba | Ca | Da |
| Blue | 0.39 | 0.33 | 0.26 | 0.20 | 0.18 | 0.18 | 0.22 | 0.27 | 0.29 |
| Green | 0.28 | 0.21 | 0.17 | 0.15 | 0.14 | 0.14 | 0.16 | 0.19 | 0.22 |
| Red | 0.17 | 0.13 | 0.11 | 0.09 | 0.09 | 0.10 | 0.11 | 0.13 | 0.17 |
| NIR | 0.17 | 0.12 | 0.10 | 0.09 | 0.08 | 0.09 | 0.10 | 0.13 | 0.21 |
| # | 1186 | 1186 | 1185 | 1158 | 1131 | 1180 | 1168 | 1173 | 1172 |

**The first four rows present the decadal trends for all 4 MISR wavelengths and 9 cameras. The second four rows represent the 95% Confidence Intervals (CI) for the corresponding trends. The final row gives the number of events for each camera.**
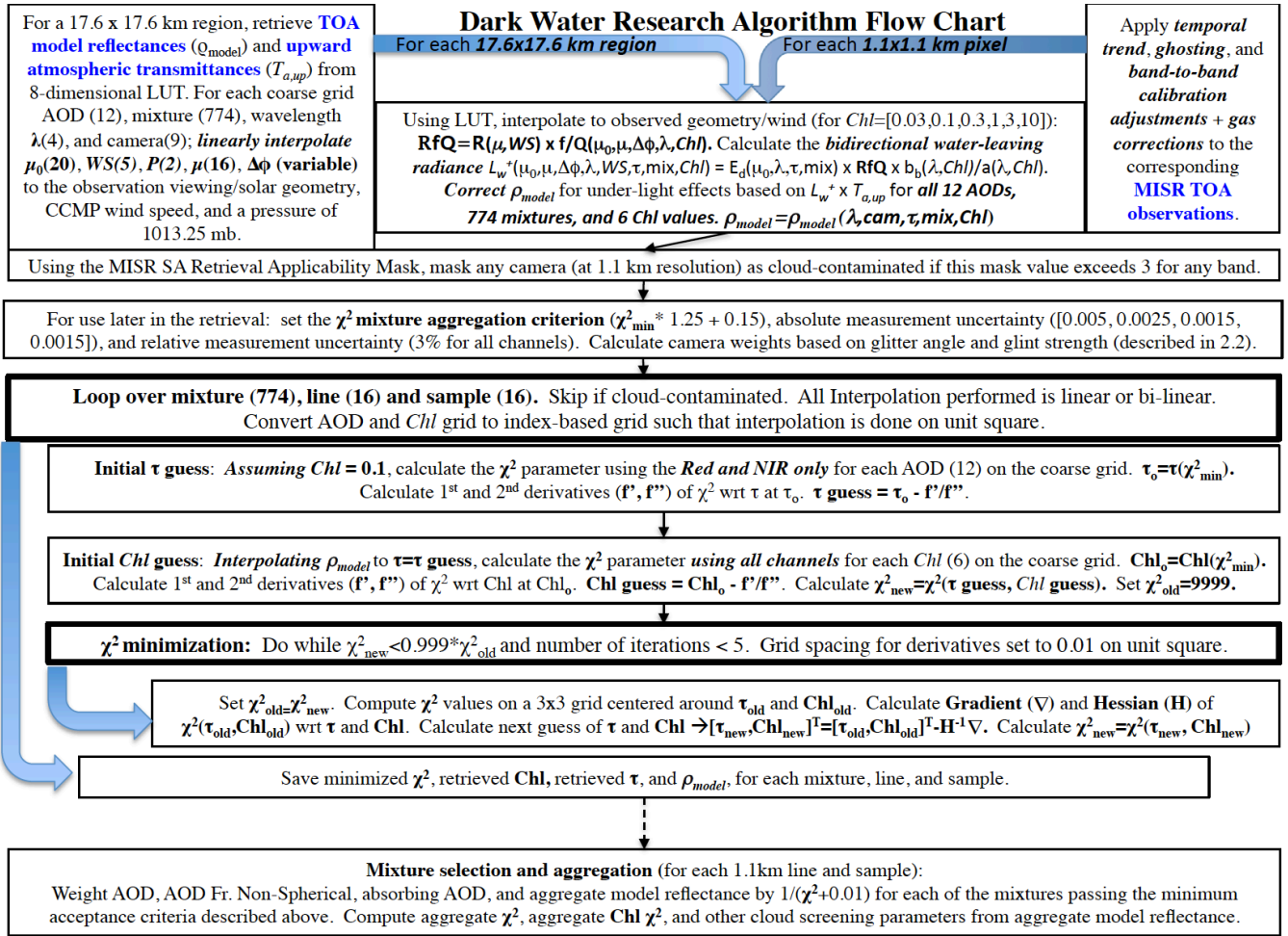
**Figure 1**

Figure 1. Flow chart describing the MISR RA aerosol/*Chl* retrieval process.
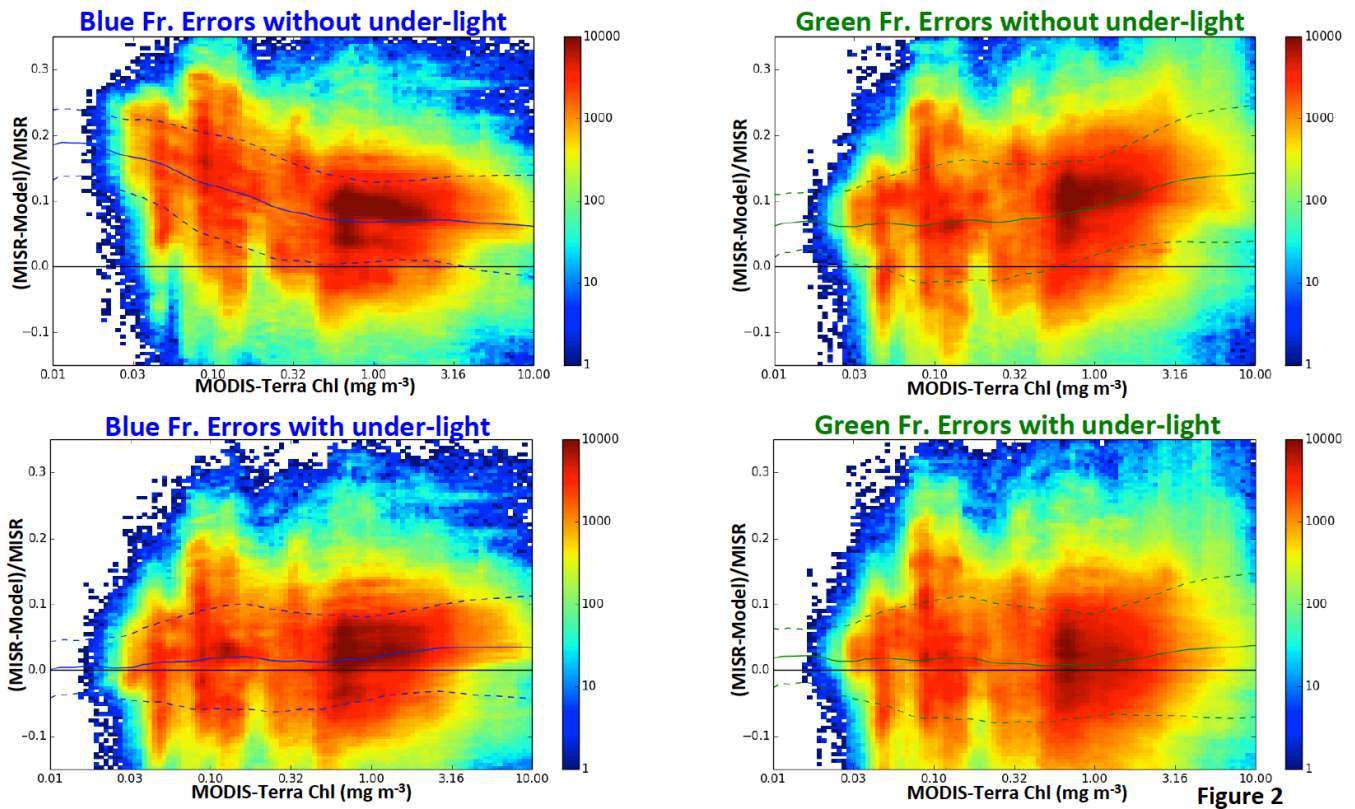
**Figure 2.** The effect of including under-light, assessed by comparing the MISR-observed TOA reflectances with model-simulated values, not including (top panels) and including (bottom panels) under-light calculated with independently retrieved MODIS *Chl* values. These joint histograms show (MISR - Model)/MISR TOA reflectance for the blue (446 nm, left) and green (558 nm, right) spectral bands, as a function of MODIS *Chl*. All glint-free cameras are aggregated for this analysis. The solid blue (or green) lines represent the smoothed mean bias, and the dashed lines indicate ± 1 smoothed standard deviation. AOD and mixture were obtained by running the RA with under-light included, based on the MODIS *Chl*, and finding the best-fitting mixture and AOD (using only the NIR band, but up to 9 cameras). Once AOD and mixture were obtained, the TOA reflectances were calculated with the forward model, both with and without under-light. Results show that including under-light dramatically lowers the bias in both the blue and green bands for all *Chl* up to 10 mgm$^{-3}$. As expected, because Chlorophyll-a strongly absorbs in the spectral response range of the MISR blue wavelength, the contribution of under-light to the TOA reflectance decreases with *Chl* in the blue, whereas it increases with *Chl* in the green due to the enhanced scattering from phytoplankton.
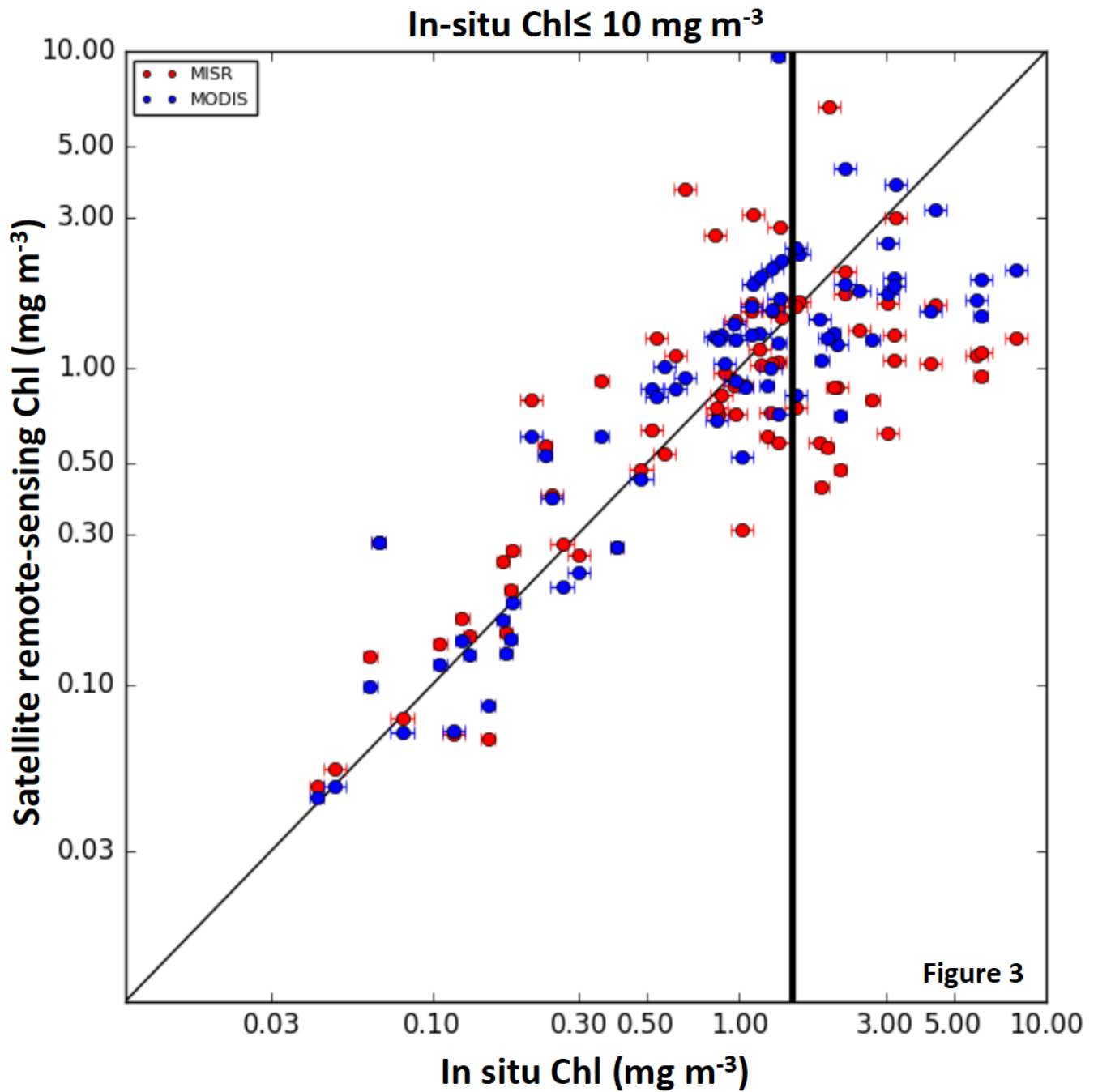
**Figure 3.** MISR (red points) and MODIS (blue) *Chl* plotted against SeaBASS validation data for $Chl_{in\ situ} \leq 10$. Results are presented if both MODIS and MISR have at least one valid retrieval in a 5×5 pixel box surrounding the central SeaBASS location. The vertical black line represents $Chl_{in\ situ} = 1.5$. We expect better-quality MISR Chl retrievals to the left of this line.
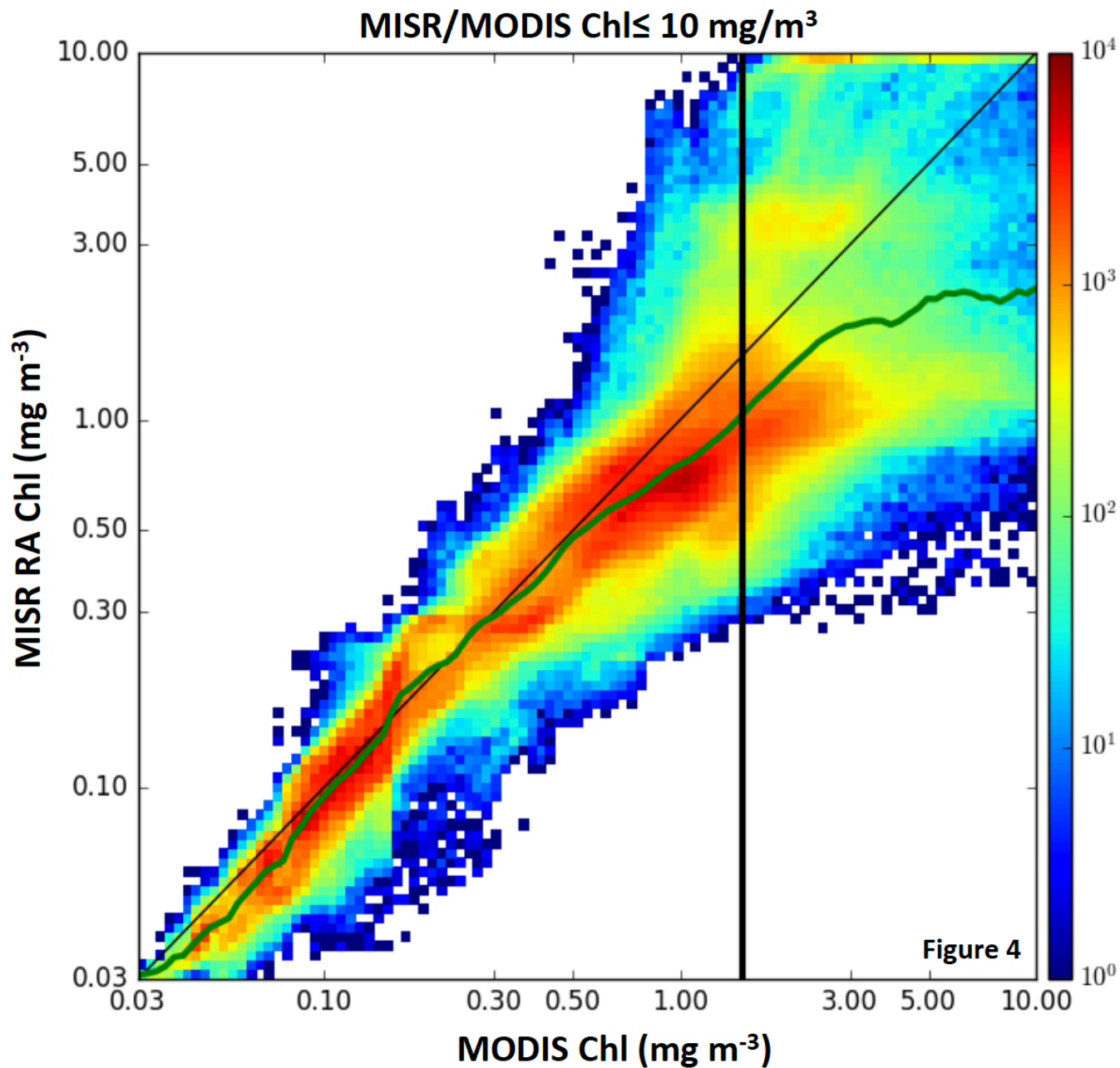
**Figure 4. MISR-MODIS *Chl* scatter-density plot for *Chl$_{MODIS}$* ≤ 10. The green line represents the mean MISR *Chl* value for each MODIS *Chl* bin, and the vertical black line represents *Chl$_{MODIS}$* =1.5. The bin size used for the green line is roughly 0.03 in log$_{10}$ space.**
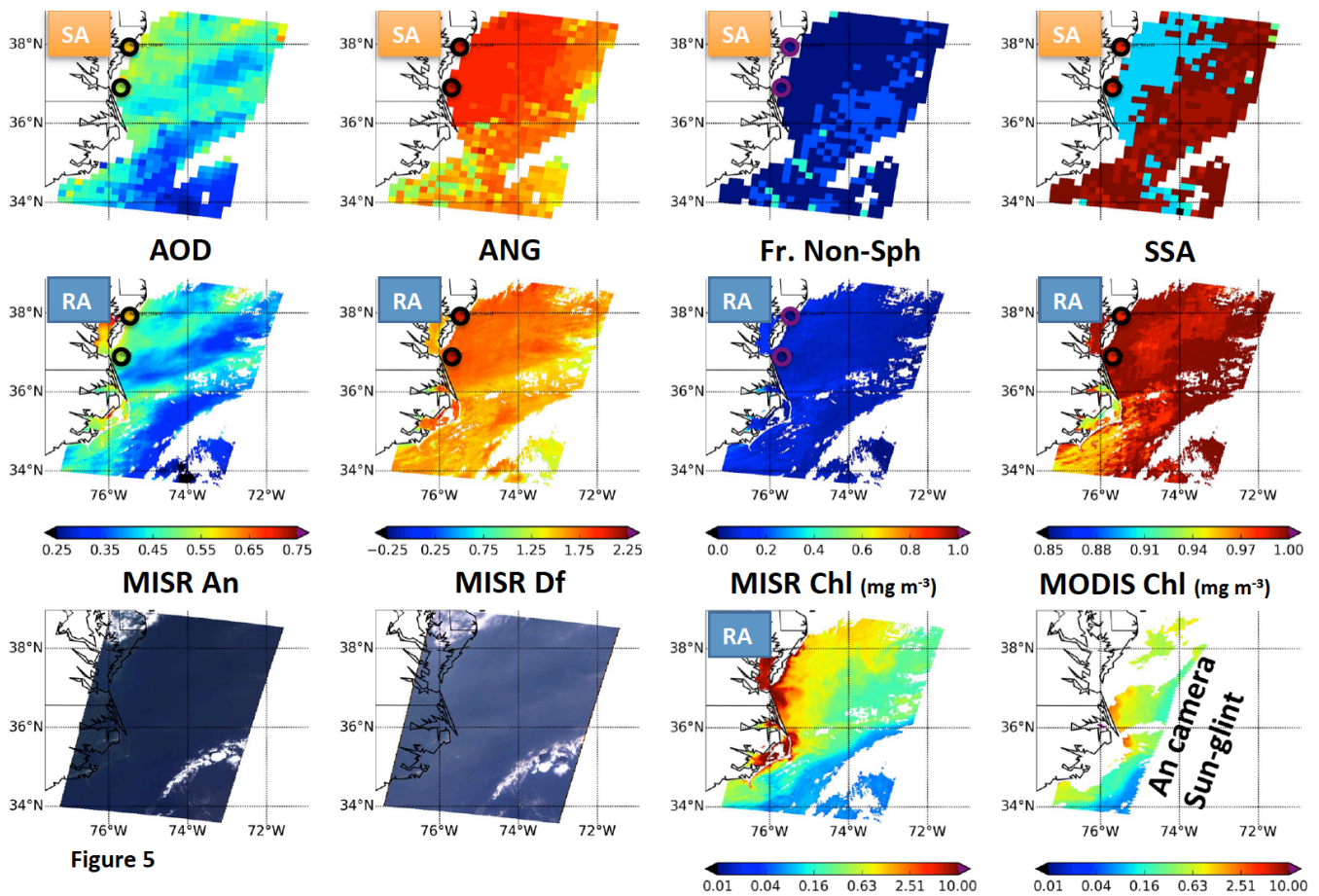
**Figure 5.** MISR imagery acquired on August 26, 2003, 15:51Z: Terra Orbit 19620, Blocks 60-63, along the US East Coast. Plots compare the MISR SA (at 17.6 km resolution, top row) to the RA that includes retrieved *Chl* (at 1.1 km resolution, row 2). AOD and particle properties correspond to the MISR green band (558 nm). AERONET direct-sun and inversion values are shown for the COVE and Wallops stations as embedded circles. AERONET Fr. Non-Sph may not be informative when aerosol extinction is dominated by the fine mode. In the lower left, MISR An and Df RGB images are shown for context. MISR-retrieved *Chl* and MODIS-retrieved *Chl* are shown in the bottom right two panels.
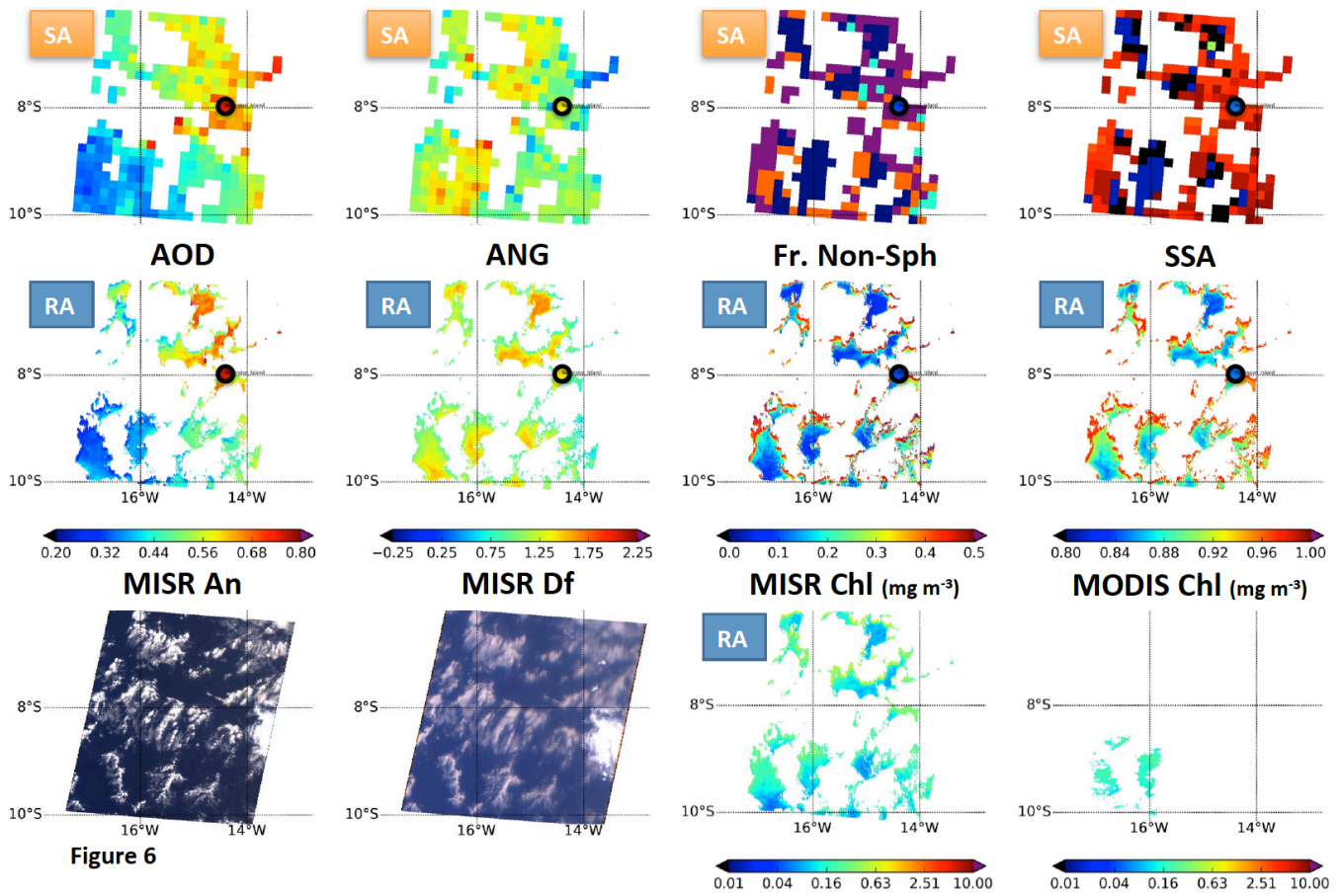
**Figure 6.** Same as Figure 5, but for data acquired on August 31, 2003, 11:26Z: Terra Orbit 19690, MISR Blocks 96-98, in the mid-south Atlantic Ocean near Ascension Island.

## Libya 4 De-seasonalization example:

**Before**               **After**

**Figure A1**

DOY               DOY
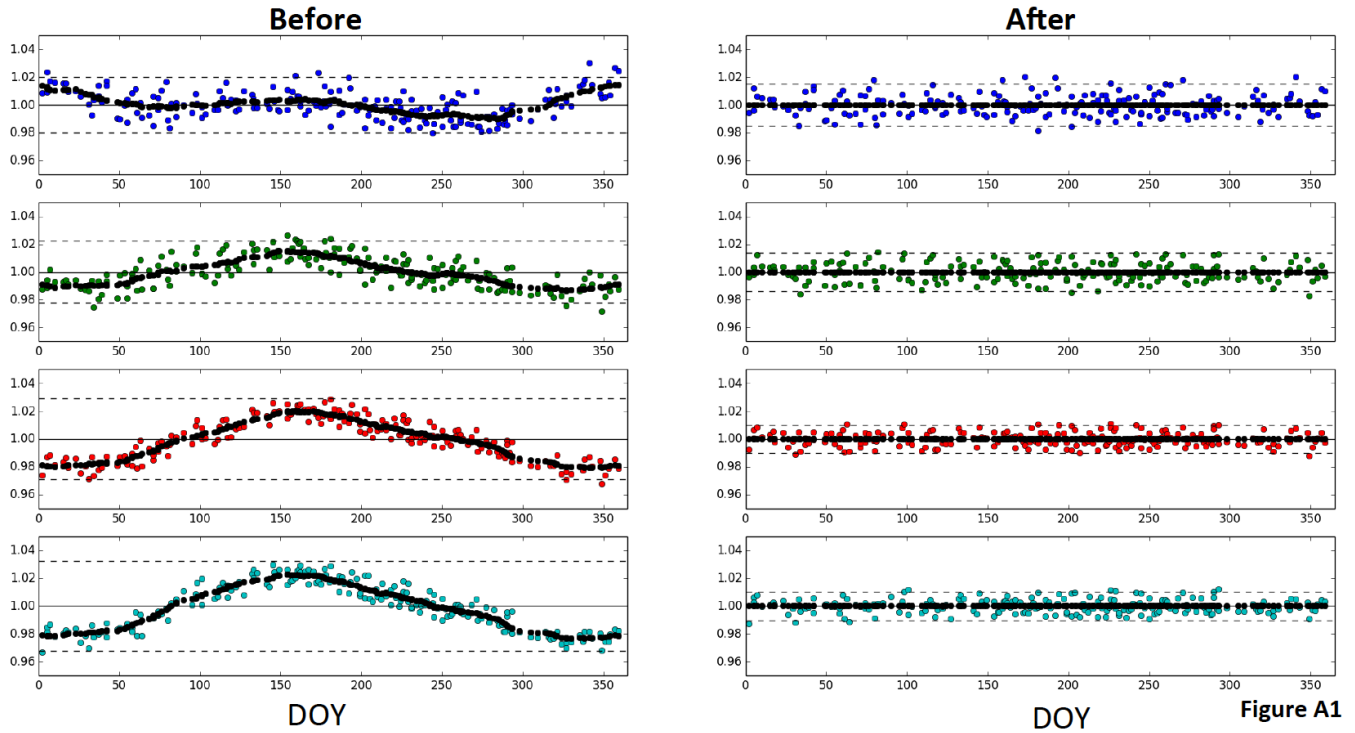
**Figure A1. De-seasonalization example for Libya 4. Data are normalized such that the mean value of each time-series is unity. Dashed black lines indicate ±2 standard deviations. The plots on the left show the MISR An (nadir camera) data for the four spectral bands, after Step 2d in Appendix A has been performed. The plots on the right show the same data after Step 3b is complete. These plots present results for only one of two separate paths covering Libya-4, and for only one of nine cameras. Similar analysis was performed for two paths for each of the three stable desert sites.**
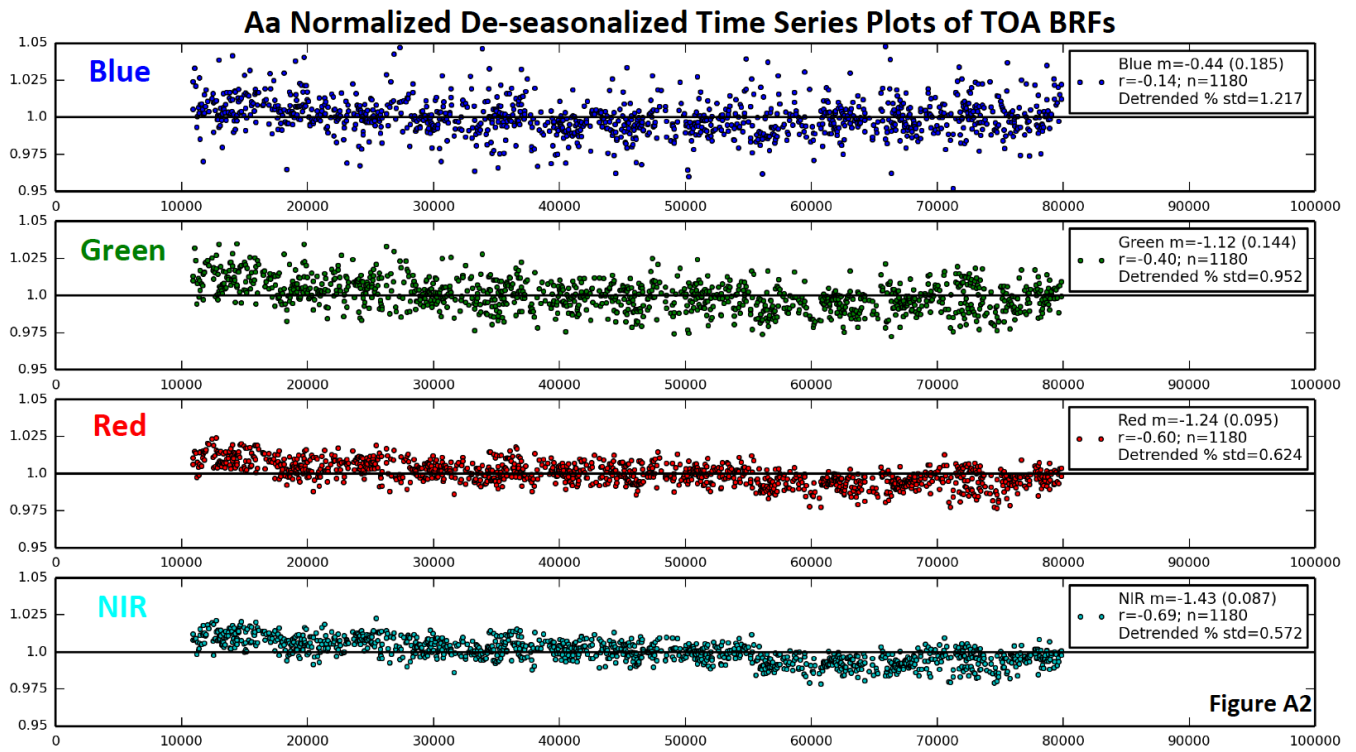
**Figure A2. Normalized, de-seasonalized TOA BRF time series plots, for the four spectral bands of the MISR Aa camera. Data are normalized such that the mean value is unity. These data present all of the data for the three desert sites used (Libya-1, Libya-4, and Egypt-1), excluding outliers, processed through Step 4b of Appendix A.**

**Figure A3.** MISR calibration drift per decade (in percent) for all four wavelengths and nine cameras. The data used to generate this plot were aggregated from three pseudo-invariant desert sites (Libya-4, Libya-1, and Egypt-1). The mean decadal trends and the 95% confidence intervals (Student's t-test) are plotted. The viewing angles associated with the MISR cameras are the following (F is forward, A is aft): DF-70.5°, CF-60.0°, BF-45.6°, AF-26.1°, AN-0.0°, AA-26.1°, BA-45.6°, CA-60.0°, DA-70.5°.